Eur. Phys. J. D **38**, 151–162 (2006)
DOI: 10.1140/epjd/e2006-00029-y

THE EUROPEAN PHYSICAL JOURNAL D

Photolysis of NO_2 at multiple wavelengths in the spectral region 200–205 nm

A velocity map imaging study

A.M. Coroiu[1], D.H. Parker[1,a], G.C. Groenenboom[2], J. Barr[3], I.T. Novalbos[3], and B.J. Whitaker[4]

[1] Department of Molecular and Laser Physics, University of Nijmegen, 6500 GL Nijmegen, The Netherlands
[2] Institute of Theoretical Chemistry, University of Nijmegen, 6525 ED Nijmegen, The Netherlands
[3] Facultad de Ciencias, Dpt. Qumica Fisica, I. F. Quimica, Universidad Compultense, Madrid, Spain
[4] School of Chemistry, University of Leeds, Leeds LS2 9JT, UK

Received 8 August 2005
Published online 8 February 2006 –

Abstract. A study of the photodissociation dynamics of NO_2 in the 200–205 nm region using resonance enhanced multiphoton ionization (REMPI) in conjunction with the velocity map imaging technique is presented. We chose this region because it allowed the use of a single laser to photodissociate the NO_2 molecule and probe both the $O(^1D_2)$ fragment using (2+1) REMPI via the $3p'^1P_1$ state at 2×205.47 nm and the $3p'^1F_3$ state at 2×203.5 nm, and the $O(^3P_J)$ fragments using (2+1) REMPI via the $4p\ ^3P_J$ states around $2 \times \sim$200 nm. Translational energy and angular distributions are extracted from the $O(^1D)$ and $O(^3P)$ product images. A growth in the population of highly excited vibrational levels of the NO $X(^2\Pi)$ co-fragment is found as the dissociation wavelength decreases. These are compared with similar trends observed previously for other triatomic O-atom containing molecules. Detailed information on the electronic angular momentum alignment of the $^1D_2$ state is obtained from analysis of the polarization sensitivity of the $O(^1D)$ images using the two resonant intermediate states. The angular dependence of the potential energy in the exit channels is examined using long-range quadrupole-dipole and quadrupole-quadrupole interaction terms, from which molecular-frame multipole moments of the total angular momentum of the recoiling O atoms have been calculated. Comparison with the experimentally derived multipole moments is used to help provide insight into the dissociation mechanism.

PACS. 31.50.Df Potential energy surfaces for excited electronic states – 33.80.Gj Diffuse spectra; predissociation, photodissociation – 34.50.Lf Chemical reactions, energy disposal, and angular distribution, as studied by atomic and molecular beams

1 Introduction

The NO_2 molecule is photolytically active in the UV spectral region (Fig. 1) where it is known to dissociate through two spin conserved channels according to reactions (1) and (2):

$$NO_2\,\tilde{X}(^2A_1) + h\nu \rightarrow NO(X\ ^2\Pi) + O(^3P_J) \qquad \lambda < 397.86\ \text{nm}, \quad (1)$$

$$NO_2\,\tilde{X}(^2A_1) + h\nu \rightarrow NO(X\ ^2\Pi) + O(^1D_2) \qquad \lambda < 243.85\ \text{nm}. \quad (2)$$

The NO–O bond energy $D_0(\text{NO}-\text{O}) = 25128.5 \pm 0.2\ \text{cm}^{-1}$ was accurately obtained by Jost et al. [1] using a laser-induced fluorescence method and near-threshold photolysis. The $O(^1D_2)$ electronic level of channel (2) lies

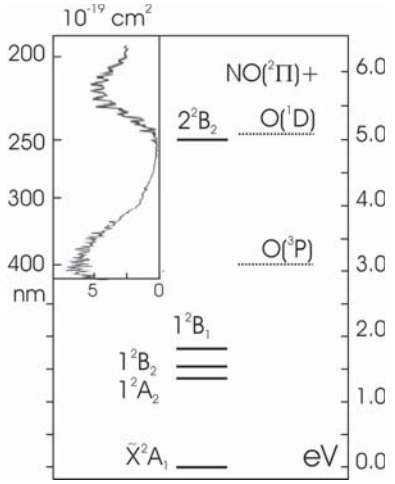

Fig. 1. Schematic energy level diagram of NO_2 electronic states, dissociation limits, and the corresponding absorption spectrum, adapted from reference [20].

[a] e-mail: parker@science.ru.nl

15867.9 cm^{-1} above the $O(^3P_2)$ ground state of atomic oxygen produced in channel (1), and spin-orbit splitting of the $NO(X\ ^2\Pi_{3/2,1/2})$ state is 119.82 cm^{-1}.

Numerous previous experimental studies of NO_2 photodissociation have measured the energy disposal and $O(^3P_J)$ $J = 2, 1, 0$ branching ratios of the fragments produced via channel (1). For example, Busch and Wilson [2, 3] worked with an effusive NO_2 beam which was photolysed using a doubled ruby laser at 347.1 nm and detected the resulting fragments using time-of-flight mass spectrometry. They found equal populations of $NO(v = 0, 1)$ and significant rotational excitation. Zacharias et al. [4], working at 337.1 nm found an inverted vibrational population distribution peaking at $v_{max} = 2$, the maximum level energetically possible $NO(v)$ level. Slanger and coworkers [5] investigated the internal energy distribution of NO following NO_2 photodissociation in the 248–290 nm region and found a great propensity for the excess available energy to go into NO vibrational excitation. At 248 nm $v_{max} = 8$ and the distribution was found to peak sharply at $v = 7$. Miyawaki et al. [6] reported the spin-orbit state distribution of the $O(^3P_J)$ fragments produced during NO_2 photodissociation at 212, 266, 337 and 355 nm. Their experiments employed a supersonic jet of NO_2 and LIF detection of $O(^3P_J)$ fragments. They found an $O(^3P_J)$ distribution of $J = 2{:}1{:}0 = 1.00{:}0.19{:}0.03$ at 266, 337 and 355 nm, while the photolysis at 212 nm yielded 1.00:0.35:0.08 (a statistical distribution would be 1.00:0.60:0.20).

Other previous experimental studies of NO_2 photodissociation have measured the angular distributions of the fragments produced via channel (1). For instance, Busch and Wilson [3] showed by angular distribution measurements that photo-absorption occurs to the 1^2B_2 electronic state, a state which is strongly coupled to the $^2A_1$ ground electronic state and which exhibits fast predissociation to NO ($X\ ^2\Pi_{1/2,3/2}$) and $O(^3P_J)$ [7]. When using linearly polarized light, the photofragment angular distribution for NO_2 follows the well known equation, $I(\theta) = (1/4\pi)[1+\beta P_2(\cos\theta)]$, where θ is the angle between the photolysis laser polarization and the fragment velocity vector, and β is the anisotropy parameter. If the molecule dissociates quickly relative to its rotational lifetime, then β is given by the simple equation $\beta = 2P_2(\cos\chi)$ where χ is the angle in the molecular frame between the transition dipole moment and the velocity vector of the fragment. For prompt dissociation, measurement of the spatial anisotropy parameter, β, therefore enables a determination of the geometry of the molecule at the time of dissociation, as long as the direction of the transition dipole moment is known. Since the ground state is totally symmetric ($^2A_1$), the transition dipole will have the same symmetry as the excited state. This means for a transition to a $^2B_2$ upper state the transition dipole moment will be perpendicular to the C_{2v} axis and in the plane of the molecule. Should NO_2 dissociate from the same geometry as the ground state where the O–N–O angle is 134°, then the photofragment angular distribution would be described by $\beta = 1.4$. Hradil et al. [8] investigated the photolysis of NO_2 via the 1^2B_2 upper state at 355 nm using the photofragment imaging technique. They found the same anisotropy parameter for both the $O(^3P_2)$ and NO fragments of $\beta = 1.2 \pm 0.3$ for both fragments. This value for β was significantly larger than that originally determined by Busch and Wilson. The difference could be attributed to the fact that in a thermal beam the rotational period is comparable to electronic predissociation time. The average rotational period at 370 K (the temperature of Busch and Wilson's experiments) is 224 fs compared to 5.5 ps at 15 K (the temperature of Hradil et al. experiments). Time resolved PHOFEX studies by Wittig and co-workers [9] have shown that the lifetime of the 1^2B_2 for dissociation via channel (1) falls rapidly from 50 ps at 2–3 cm^{-1} above threshold to below 7.7 ps by 25 cm^{-1} of excess energy and to less than 0.8 ps at about 800 cm^{-1} of excess energy. A study of both fragments from jet cooled NO_2 at 371.1, 354.7 and 338.9 nm was published by Demyanenko et al. [10]. They obtained the anisotropy parameter for $O(^3P_{2,1})$ from measurements of the NO fragment. From their results it was deduced that, especially with photon energies closer to threshold dissociation, β depends strongly on both the rotational and translational energy of the fragment.

In this study we excite the NO_2 molecule around 200 nm to the presumed 2^2B_2 state. In contrast to 1^2B_2 state the 2^2B_2 state is predissociative from its origin [11]. The absorption spectrum (Fig. 1) shows a progression of broad peaks above a continuum that reaches a local maximum around 220 nm. The lifetime of low lying rotational levels in the $^QR_0$ branch of the (0, 0, 0) band at an excitation energy of 40126 cm^{-1} has been measured by Tsuji et al. [12] to be 41 ps. Here, the dissociation is believed to proceed via internal conversion to the high lying vibrational states in the 1^2B_2 state leading to vibrationally excited $NO(X^2\Pi)$ + $O(^3P)$. The (0, 1, 0) and (0, 0, 2) vibrational levels 525 and 718 cm^{-1} above the (0, 0, 0) level respectively similarly lead to ground state products but the dissociation rate is much faster than the origin band (the lifetimes are 4.8 and 160 fs respectively [12,13]. The next vibrational level (1, 0, 0) of the 2^2B_2 state lies ∼300 cm^{-1} above the second dissociation limit at 243 nm (40125.85 cm^{-1}) at which channel (2) opens but the excited state lifetime, between 75 and 62 fs, is not markedly shorter than that of the (0, 0, 2) level. Some variation in the lifetimes of the subsequent three vibrational bands was noted by Tsuji and co-workers but no systematic dependence on the vibrational mode could be discerned and remained ∼100 fs as the excess energy was increased.

Besides the study of Miyawaki et al. [6] at 212 nm, there have been only a few reports of NO_2 photodissociation product state distributions at energies above the second dissociation limit. Slanger and coworkers [14] reported photodissociation at 157 nm with NO detection by LIF. They found predominantly ground-state channel (1) products with very high rotational ($N \leq 73$) and vibrational ($v \leq 21$) excitation, even though channel (2) and higher channels ($O(^1S)$ production, for example) are open at this VUV wavelength. Other studies, including the present

report, have used optical excitation in the second band covering the 240–190 nm region shown in Figure 1. In this region the $O(^1D)$ quantum yield was found by Uselman and Lee [15] to increase from 0 at 243 nm to around 0.4–0.5 in the 230–210 nm region. This finding is in agreement with the linewidth study of Tsuji et al. [12] which concluded that the predissociation rate into channel (1) was high enough to compete with that into channel (2) since the linewidths just above and below the second ionization limit were approximately the same. However, at a slightly shorter wavelength Richter et al. [16] determined the yield ratio $O(^1D)$:$O(^3P)$ to be 7:1 by monitoring the temporal profile of $O(^3P)$ production after photolysis at 212.8 nm laser light of effusive NO_2 using an N_2 or He buffer.

Shafer et al. [17] have reported (2+1) REMPI detection of $O(^1D)$ following 205.47 nm photolysis of an effusive beam of NO_2 using a single laser for both dissociation and detection. They found an anisotropy parameter $\beta = 1.32$, indicative of prompt dissociation. Ahmed et al. [18] have reported a one color experiment at ∼226 nm to dissociate NO_2 and simultaneously detect the $O(^3P_J)$ and NO fragments by (2+1) and (1+1) REMPI, respectively. NO detection provides information on both the NO + $O(^3P)$ and NO + $O(^1D)$ channels for the selected NO quantum state. They found the anisotropy parameter $\beta = 1.32$ for the $O(^3P_0)$ atom and a different value of $\beta \sim 0.6$ for the $O(^1D)$ channel. A branching ratio of $O(^1D)$:$O(^3P)$= 1.00:0.01 was extracted from the NO($v = 0$, $N = 16$) fragment image in a (1+1) REMPI process. In further work, this group has also studied the dissociation at 212.8 nm with subsequent detection of $O(^3P_J)$ fragments at 226 nm using the velocity map imaging technique [19]. Their two-laser experiment allowed the study of angular momentum alignment in the $O(^3P_{2,1})$ product ($O(^3P_0)$ has zero total angular momentum and thus no alignment) by changing the probe laser polarization. The results of reference [19] showed that the dominant mechanism responsible for the alignment is an incoherent parallel excitation of the parent molecule.

In our experiment velocity map imaging is applied to study the energy partitioning and angular distribution of the $O(^3P_J)$ and $O(^1D)$ photofragments produced by photodissociation of the NO_2 molecule at wavelengths between 200.64–205.47 nm. $O(^3P_J)$ detection takes place by (2+1) REMPI via the $1s^22s^22p^44p(^3P_J)$ Rydberg state in the ∼200 nm region instead of the usual (2+1) REMPI via the $1s^22s^22p^43p(^3P_J)$ state in the ∼226 nm region. One advantage of this detection scheme is that the wavelengths used in the standard detection method for $O(^1D_2)$ atoms [16] also fall in the same region. In a separate paper [21] we show that the polarization and J-dependent sensitivity using the $4p(^3P_J)$ state is similar to detection via the $3p(^3P_J)$ state, and the overall sensitivity is a factor of ∼7 lower. The $O(^1D_2)$ transitions are at 205.47 and 203.82 nm, via the $3p'^1P_1 - {}^1D_2$ and $3p'^1F_3 - {}^1D_2$ states, respectively. We describe here one-laser experiments where dissociation takes place at the wavelength tuned for the REMPI detection process. Using the $4p(^3P_J)$ resonance we can thus compare $O(^3P_J)$ and $O(^1D)$ data at similar dissociation energy. In reference [21] we compare yield and polarization sensitivity factors for the two $O(^3P_J)$ detections schemes and the two $O(^1D)$ schemes. Our present one-laser experiments offer very limited polarization information for $O(^3P_{2,1})$ detection. For $O(^1D_2)$ detection the $^1P_1$ and $^1F_3$ states have quite different two-photon angular-dependent alignment sensitivity for each $|m_J|$ state ($m_J = -2, -1, 0, 1, 2$). Polarization information can thus be extracted by comparing the two detection pathways following the assumptions and methods introduced by Mo and Suzuki [22].

Photodissociation studies of other O-atom containing triatomic molecules such as O_3 [23], N_2O (Neyer et al. [24], Teule et al. [25]), SO_2 [26], OCS [27] and OClO [28] have been reported, which can be compared with the present data. In particular, we find that an m_J-dependent anisotropy parameter is necessary in the alignment analysis of our $O(^1D)$ images. We use a long-range quadrupole-dipole and quadrupole-quadrupole interaction analysis similar to that used for related studies of N_2O and SO_2. From this analysis the molecular-frame multipole moments of the total angular momentum of the recoiling O atoms have been calculated. In contrast to NO_2 and SO_2, no potential energy surfaces are available for states correlating to the second dissociation limit of NO_2. The standard approach of comparing the adiabatic and diabatic limits for connecting the optically excited state to the dissociation products is thus not possible at this moment in the case of NO_2. Instead, we compare the measured product distribution with those predicted for different adiabatic states combining the $O(^1D)$ and $NO(^2\Pi)$ sub-units in C_s symmetry.

In Section 2, we described the experimental set-up used. In Section 3, we present the measured images, their data analysis and results. In Section 4, we discuss the long-range model. In Section 5, we summarize our results for this one-laser study.

2 Experimental set-up

The experiment was performed on a new on-axis velocity map imaging set-up based on the design of Eppink and Parker [30]. Briefly, it consists of two vacuum chambers evacuated to 2×10^{-7} Torr: the source chamber and the detection chamber, which are separated by a gate valve. During the experiment the gate valve is open and the chambers are connected by a 2 mm skimmer on axis with respect to the electrostatic lens. Optical access to the detection chamber is provided between the repeller and extractor lenses by 4 VUV windows. This allows two laser beams to propagate perpendicular to each other and to the TOF axis. The electrostatic lens accelerates the charged particles produced by laser ionization through a 34 cm field-free TOF tube to the position sensitive detector.

The photolysis light is generated by a dye laser operating at ∼600 nm, pumped by the 2nd harmonic of a Nd:YAG laser. By frequency tripling using a KDP crystal for doubling followed by mixing in a BBO crystal, wavelengths were selected at 200.64 nm, 200.96 nm, 201.1 nm,

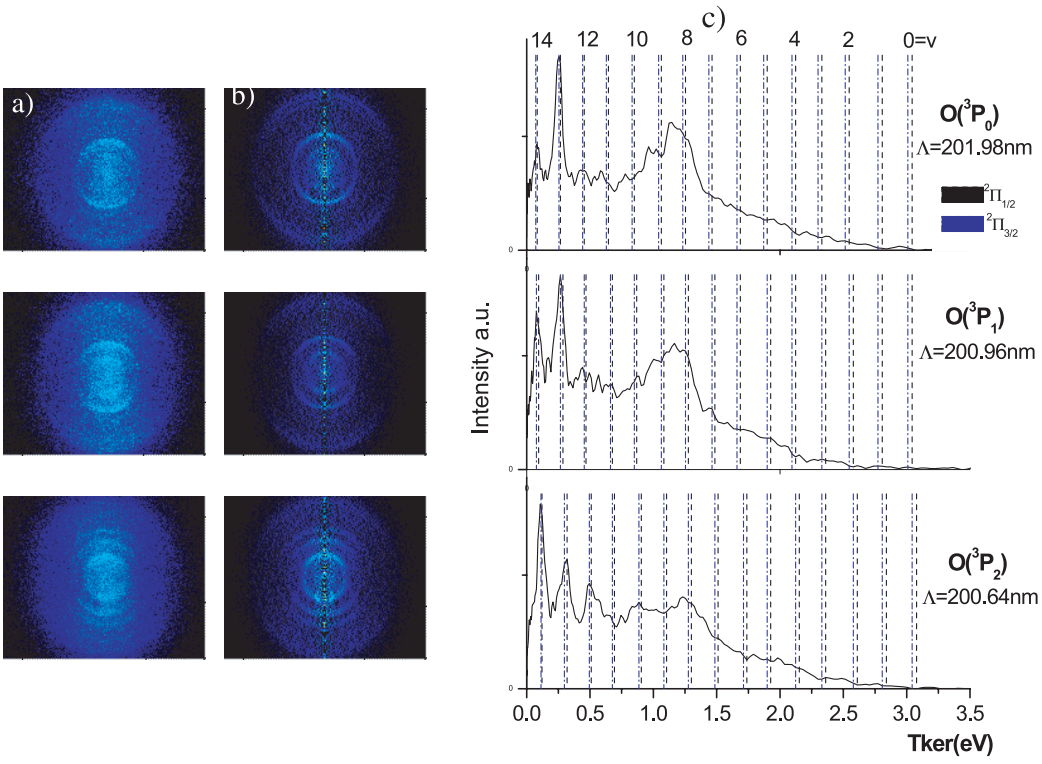

Fig. 2. (a) Raw image and (b) 2-D slices of the reconstructed 3-D recoil distribution of $O(^3P_2)$, $O(^3P_1)$ and $O(^3P_0)$ atoms resulting from photolysis of jet-cooled NO_2 at 200.64, 200.96 and 201.1 nm; (c) The corresponding translational energy distributions. A colour version of the figure is available online at `http://www.eurphysj.org`.

203.8 nm and 205.47 nm. Each of these chosen wavelengths is used to photodissociate and subsequently probe the oxygen product in a one-laser experiment.

A pulsed supersonic beam of 0.5% NO_2 in He is directed along the TOF axis. In order to avoid NO_2 clustering a 0.4 bar backing pressure of the molecular beam was applied. The charged photofragments were then projected onto a gated dual microchannel plate (MCP) assembly, followed by a phosphor screen. The CCD camera (PixelFly, size: 640 × 480 pixels) records the 2D distribution on the phosphor screen. Mass selectivity is obtained by gating the front MCP. Typically, 5000–10000 laser shots were averaged to collect the raw 2D image. The full 3D fragment distribution was then reconstructed from the raw 2D image by utilizing an inversion algorithm [30]. The inverted image represents a slice through the middle of the reconstructed 3D fragment distribution from which fragment translational distribution is extracted.

The 200–205 nm laser light (∼1 mJ/pulse, 0.5 cm^{-1} bandwidth) was focused onto the molecular beam by a 20 cm lens. Due to the Doppler width of the oxygen fragments, the probe laser frequency was scanned over the entire Doppler profile to ensure that all product velocities were detected with equal sensitivity.

3 Results and discussion

3.1 $O(^3P_J)$ detection from photodissociation of NO_2 at 200.64, 200.96, and 201.98 nm

UV photodissociation of NO_2 induced by a pulsed laser tuned to the REMPI transition for $O(^3P_2)$ detection at 200.64 nm initiates the photodissociation process:

$$NO_2 + h\nu_{200.64\ \mathrm{nm}} \rightarrow NO(X^2\Pi_{1/2}) + O(^3P_2) + 3.116\ \mathrm{eV}. \quad (3)$$

Figure 2a displays raw O^+ images, which are 2-D projections of the O^+ 3-D Newton spheres, taken at three different wavelengths: 200.64 nm, 200.96 nm and 201.098 nm, used for $O(^3P_J)$ REMPI for $J = 2$, 1 and 0, respectively. Abel-transformed images are shown in Figure 2b. All $O(^3P_J)$ images were taken in the same condition of backing pressure, ∼0.4 bar, and laser intensity, 0.9 mJ/pulse. The laser electric field polarization direction E is horizontal in the laboratory frame (i.e. parallel with the surface of the detector) which is necessary for the reconstruction of the 3D velocity distribution from the original 2D ion data. Ion intensities in these representations increase from black to white.

The relative $J = 2{:}1{:}0$ yield found by integrating the entire images under the same conditions was 1:0.02:0.02, in large disagreement with a statistical 1:0.6:0.2 ratio. It appears that the wavelength used for REMPI of O^3P_2 at ∼200 nm is accidentally resonant with an absorption peak of our jet-cooled NO_2 sample. Because the general appearance of the three O^3P_J images is similar, we suggest that this is a simple intensity effect and does not significantly change the angular or kinetic energy information.

In each of the images several well resolved sharp rings peaking at radii close to the center of the detector are discernible. The high intensities observed at small pixel radii indicate that the major fraction of the $O(^3P_2)$ atoms

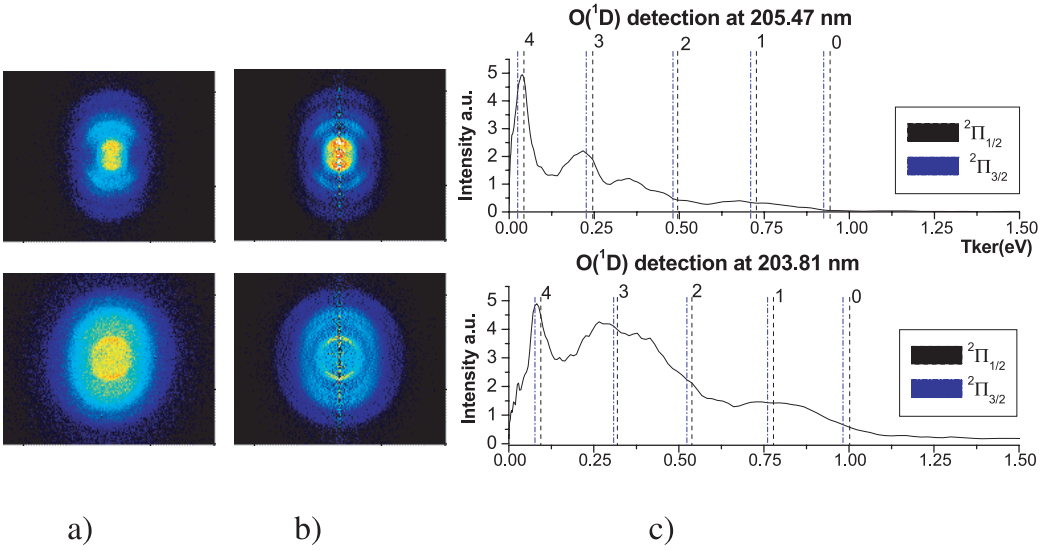

Fig. 3. (a) Raw image and (b) 2-D slices from reconstructed 3-D recoil distribution of $O(^1D_2)$ atoms resulting from photolysis of jet-cooled NO_2 recorded by 2+1 REMPI via the $^1P_1$ and $^1F_3$ Rydberg states at an excitation wavelength of 205.47 and 203.81 nm respectively; (c) The corresponding translational energy distributions. A colour version of the figure is available online at `http://www.eurphysj.org`.

are released with very low velocities in the dissociation process.

In Figure 2c the vibrational level of the NO co-fragment is indicated in the $O(^3P_2)$ translational distribution. The inner ring of the image corresponds to $v_{max} = 14$, the highest possible $NO(^2\Pi)$ vibrational level. Rings for $v = 13$ and $v = 12$ are also present and the largest diameter ring corresponds to $NO(^2\Pi)$ $v \sim 7$. Note that the 123.14 cm^{-1} $NO(^2\Pi_{3/2} \leftarrow {}^2\Pi_{1/2})$ spacing should result in a splitting of the rings which is not resolved in this study, most likely due to overlapping rotational levels. The vibrational spacing observable in the kinetic energy distributions are in good agreement with the known vibrational constants of $NO(X^2\Pi_{1/2,3/2})$ from the *NIST* database. Many of the vibrational levels are well-resolved, especially those corresponding to the low fragment kinetic energy distribution [25]. Also apparent is the lower rotational energy spread for the high vibrational levels $v = 12$–14 compared the lower levels $v = 7$–11. The $O(^3P_0)$ image reported by Ahmed et al. for photodissociation of NO_2 at 226 nm is quite broad and without structure, similar to the outer rings $v = 7$–11 of our image at 200 nm [18]. At our higher excitation energy we see the growth of a new set of low kinetic and rotational energy, maximally vibrationally excited NO molecules, reminiscent of our OClO study [28] where, again at the blue edge of the absorption spectrum, extremely highly vibrationally exited $OCl(v = 22)$ was the only product observed. Similar effects are seen for ultraviolet photodissociation of ozone [23], where highly vibrationally excited $O_2X^2\Sigma_g^-(v > 26)$ is observed for photodissociation at the blue edge of the absorption spectrum.

Angular information from these $O(^3P_J)$ images is complicated by the alignment sensitivity of the linearly polarized detection laser. If we separate the high ($v = 14$–12) and low ($v = 11$–7) vibrational components then the anisotropy parameter, β, determined from by fitting the experimental data using $I(\theta) = (1/4\pi)[1 + \beta P_2 \cos\theta]$, was found to be $\beta(J = 2{:}1{:}0) = 0.94{:}0.83{:}0.55$ for $v = 14$–12, and $\beta(J = 2{:}1{:}0) = 1.04{:}1.16{:}1.00$ for $v = 11$–7. Because our experiment only employs a single laser we are not at liberty to independently change the polarisation of the photolysis and probe photons. Consequently, β is only meaningful in our experiment for the $J = 0$ component, where we find for the comparable $v = 11$–7 band a slightly lower value $\beta = 1.00$ at 200 nm than the value of $\beta = 1.30$ found by Ahmed et al. at 226 nm [18]. A two-color experiment with different polarization geometries such as that of reference [18] would yield a more complete picture of the dissociation dynamics for the $O(^3P_J)$ channel at ∼200 nm.

3.2 $O(^1D)$ detection produced via photodissociation of NO_2 at 205.47 and 203.81 nm

UV photodissociation of NO_2 induced by a pulsed laser tuned to the REMPI transition for $O(^1D)$ detection at 205.47 nm initiates the photodissociation process:

$$NO_2 + h\nu_{205.47\ nm} \rightarrow NO\left(X^2\Pi_{1/2,3/2}\right) + O\left(^1D\right) + 0.95\ eV. \quad (4)$$

Figure 3a displays raw O^+ images taken at 205.47 nm and 203.81 nm, used for $O(^1D)$ REMPI via the $3p'^1P_1{-}^1D_2$ and $3p'^1F_3{-}^1D_2$ states, respectively. Abel-transformed images are shown in Figure 3b. The translational distribution for $O(^1D)$, Figure 3c, shows peaks corresponding to vibrational levels 0–4 of the NO co-fragment. The most populated vibrational level of $NO(^2\Pi_{3/2}, {}^2\Pi_{1/2})$ is $v = 4$ followed by $v = 3$ (see Figs. 3b and 3c). Similar to all previous studies of channel (2) NO_2 photodissociation, a highly inverted vibrational distribution is observed where the maximum possible vibrational level is the most populated.

The width of the peaks shown in Figure 3 provides information about the rotational energy of the NO co-fragment. Gaussian fits to the $O(^1D_2)$ translational energy distribution recorded via the $^1P_1$ Rydberg state are shown in Figure 4 and Table 1.

Table 1. Gaussian fit parameters for the O(^{1}D) (via ^{1}P) translational energy distribution shown in Figure 4.

NO(v)[a]	Peak area (a.u.)[b]	Energy (eV)[c]	Calc. energy(eV)[d]	Width (eV)[e]
4	3.8	0.026	0.026	0.06
3	2.6	0.213	0.249	0.09
2	1.5	0.35	0.474	0.095
1	0.6	0.52	0.703	0.1
0	0.8	0.68	0.936	0.17

[a] Vibrational levels for NO co-fragment reflected in the O(^{1}D) image. [b] The area of the Gaussian-fit for each vibrational level. [c] Fitted peak center position. [d] Calculated energy levels using NO($J = 0$) constants from NIST. [e] Half-widths of the fitted peaks.

Table 2. (O^{1}D$_2$) measured values of anisotropy parameter β for several vibrational states of NO.

product/nm	β (NO, $v = 4$)	β (NO, $v = 3$)	β (NO, $v = 2$)	β (NO, $v = 1$)	β (NO, $v = 0$)
O(^{1}D$_2$)/ 205 nm	0.5	1.1	1.0	–	–
O(^{1}D$_2$)/203 nm	0.3	0.3	0.6	0.6	0.3

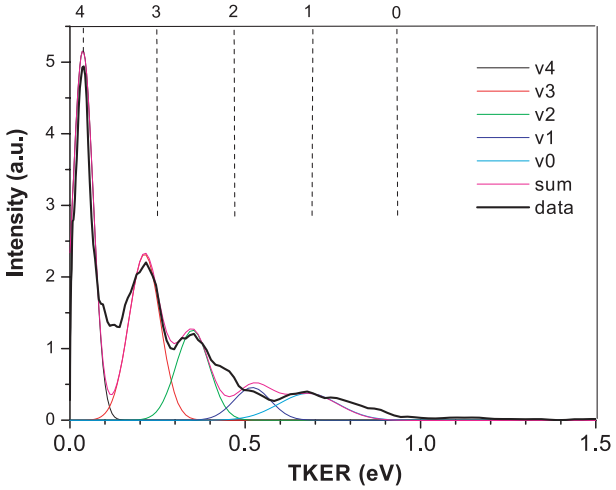

Fig. 4. Gaussian representation fit to the NO vibrational distribution determined from the O(^{1}D) kinetic energy distribution measured at 205.47nm shown in Figure 3c.

The results given in Figure 3b and 3c reveal a noticeable change in the ion intensities. In both situations Figure 3c shows intensities and widths for the lowest fragments which are more or less the same. At 203.8 nm dissociation, for the more energetic fragments the intensities and the widths of these peaks are higher. Also, at 203.8 nm we found $\beta = 0.3$ (see Tab. 2).

Both O(^{1}D$_2$) images show a broad translational energy distribution in the image, caused by the variable amount of rotational energy taken up by the NO fragment. Compared to the ^{1}F$_3 \leftarrow {}^1$D$_2$ image (recorded at 203.81 nm), the angular distribution of the ^{1}P$_1 \leftarrow {}^1$D$_2$ image (recorded at 205.47 nm) is more peaked along the vertical axis, and shows a dimple on the the horizontal axis. The differences in the angular distribution in the O(^{1}D$_2$) images using different detection schemes arises from the variation in the detection probabilities for the various m-levels in the two ionization routes. For analysis, the Abel-inverted images are divided into shells with different radii corresponding to a range of translational energies, where each shell corresponds roughly to the fitted Gaussians. The results are summarized in Table 2. Each shell corresponds to a range of rotational levels in the NO fragment.

4 Ab initio calculation and semi-classical model

4.1 Polarization effects in the velocity map image

Our interpretation of the O(^{1}D) imaging results is based on the model of Mo and Suzuki [22,31] which we summarize here. The observed ion angular distribution is written as the product of the photofragment angular recoil distribution (I_{rec}) and the detection efficiency (I_{det})

$$I_{ion}(\theta) \propto I_{rec}(\theta) I_{det}(\theta), \tag{5}$$

where θ is the angle between the photolysis laser polarization $\vec{\varepsilon}$ and the fragment velocity $\vec{v}$. The fragment distribution for a one photon transition [32] is given by

$$I_{rec}(\theta) = \frac{1}{4\pi} \left[1 + \beta_v P_2(\cos\theta)\right], \tag{6}$$

where $P_2(z) = 3z^2/2 - 1/2$ is the second order Legendre polynomial and $-1 \leq \beta_v \leq 2$ is the anisotropy parameter, which depends on the vibrational quantum number v of the co-fragment. The detection efficiency depends on the polarization of the photofragment with respect to the polarization of the probe laser [31]:

$$I_{det}(\theta) = \sum_k \rho^{(k)}_{0,PF} P_k(J_f, J_i). \tag{7}$$

where the $P_k(J_i, J_f)$ are J dependent line strength (geometric) factors and the $\rho^{(k)}_{0,PF}$ are the zero components of density matrix multipole moments of rank k [33] in the reference frame defined by the probe laser polarization

(PF - probe frame). For a two photon transition, the index k runs through even numbers from 0 to 4. For linearly polarized light ($s = 0$), where the initial and final atomic angular momenta are different, i.e., $J_i \neq J_f$, and for circularly polarized light ($s = \pm 1$) Mo and Suzuki [31] give an analytic expressions involving $3j$ and a $6j$ symbols for the line strength factors. As they point out, in many practical applications, including ours, only the relative ratio of the geometrical factors with respect to that for $k = 0$ is actually needed:

$$\tilde{P}(J_f, J_i) = P_k(J_f, J_i)/P_0(J_f, J_i) = 5\sqrt{2k+1} \times \sqrt{2J_i+1}(-1)^{J_i+J_f} \begin{pmatrix} 2 & 2 & k \\ 2s & -2s & 0 \end{pmatrix} \begin{Bmatrix} J_i & J_i & k \\ 2 & 2 & J_f \end{Bmatrix}. \quad (8)$$

In the present experiment the $O(^1D_2)$ atoms are detected at 205.47 nm through the $3p'^1P_1 \leftarrow {}^1D_2$ two photon resonance, for which we have and $\tilde{P}_2(1,2) = -\sqrt{5/14} = -0.598$ and $\tilde{P}_4(1,2) = -\sqrt{8/7} = -1.069$. We also used the $3p'^1F_3 \leftarrow {}^1D_2$ transition at 203.81 nm for which we have $\tilde{P}_2(3,2) = \sqrt{160/343} = 0.683$ and $\tilde{P}_4(3,2) = -\sqrt{9/686} = -0.115$.

The zero component of the rank k multipole moments in the probe frame, $\rho^{(k)}_{0,PF}$, are related to the multipole moments in the recoil velocity frame (RF) $\rho^{(k)}_{q,RF}$ through

$$\rho^{(k)}_{0,PF} = \sum_{q=-k}^{k} \rho^{(k)}_{q,RF} C_{kq}(\theta, \phi), \quad (9)$$

where the C_{kq} are modified spherical harmonics and θ, ϕ are the polar angles of the recoil velocity $\vec{v}$ in the probe frame, which in the present one-laser experiment has $\vec{\varepsilon}$ along the Z-axis. To limit the number of degrees of freedom in our theoretical model of the dissociation to be described below we will make the following additional assumptions about the atomic angular distribution [22]: (1) the distribution is cylindrically symmetric around the recoil velocity $\vec{v}$ and (2) the distribution is independent of $\vec{v}$. With these assumptions only the $q = 0$ component of $\rho^{(k)}_{q,RF}$ is nonzero and it can be expressed in terms the recoil frame m state fractional population f_m as

$$\rho^{(k)}_{0,RF} = \sum_{m=-J_i}^{J_i} (-1)^{J_i - m} \sqrt{2k+1} \begin{pmatrix} J_i & k & J_i \\ -m & 0 & m \end{pmatrix} f_m. \quad (10)$$

Note that, because of the symmetry of the 3-j symbol, $\rho^{(k)}_{0,RF}$ can be re-expressed in terms of $p_0 = f_0$ and $p_m = f_m + f_{-m}$ with $m > 0$. Combining equations (5–7) with equation (9) and using $C_{k,0}(\theta, \phi) = P_k(\cos\theta)$ we can express I_{ion} as

$$I_{ion}(\theta) \propto [1 + \beta_v P_2(\cos\theta)] \sum_k \rho^{(k)}_{0,RF} \tilde{P}_k(J_f, J_i) P_k(\cos\theta) = \sum_l c_l P_l(\cos\theta). \quad (11)$$

Expanding the product of Legendre polynomials using

$$P_2(z) P_k(z) = \sum_{l=\max(0,k-2)}^{k+2} |\langle 20k0|l0\rangle|^2 P_l(z) \quad (12)$$

we find

$$c_l = \rho^{(l)}_0 \tilde{P}_l(J_f, J_i) + \beta_v \sum_k |\langle 20k0|l0\rangle|^2 \rho^{(k)}_{0,RF} \tilde{P}_k(J_f, J_i), \quad (13)$$

for which the non-zero terms are

$$\begin{bmatrix} c_0 \\ c_2 \\ c_4 \\ c_6 \end{bmatrix} = \begin{bmatrix} 1 & \frac{1}{5}\beta_v & 0 \\ \beta_v & 1 + \frac{2}{7}\beta_v & \frac{2}{7}\beta_v \\ 0 & \frac{18}{35}\beta_v & 1 + \frac{20}{77}\beta_v \\ 0 & 0 & \frac{5}{11}\beta_v \end{bmatrix} \begin{bmatrix} \rho^{(0)}_{0,RF} \\ \tilde{P}_2(J_f, J_i)\rho^{(2)}_{0,RF} \\ \tilde{P}_4(J_f, J_i)\rho^{(4)}_{0,RF} \end{bmatrix}. \quad (14)$$

Since the absolute intensities are not determined, the experimental data consists of the moments $\tilde{c}_l = c_l/c_0$ for $l = 2, 4, 6$ for the two detection schemes, i.e., there are six independent parameters for each dissociation channel.

4.2 Electrostatic model for fragment polarization

To interpret the fragment polarization we apply a model similar to one developed previously to describe the photodissociation reactions $N_2O + h\nu \rightarrow N_2 + O(^1D_2)$ [25] and $SO_2 + h\nu \rightarrow SO(^3\Sigma^-) + O(^3P_J)$ [26]. In this model we compute the adiabatic electronic wave functions for the $O(^1D_2)$ atom as a function of the Jacobi angle γ (with $\gamma = 0$ corresponding to linear $ON\cdots O$) for some value of the distance R_c between the O atom and the center of mass of the NO moiety. For the atom we include the five degenerate $^1D_2$ states $|\lambda = 2, \mu\rangle, \mu = -\lambda, \cdots, \lambda$ and we only consider first order electrostatic interactions. Since the NO molecule is produced in a $^2\Pi$ state each atomic state gives rise to two potential energy surfaces of A' and A'' symmetry which are coupled by spin-orbit interaction. In the experiment, however, the two spin-orbit states of the NO fragment are not resolved and hence we compute the multipole moments of NO that are used in the model by taking the average over the two Π components, effectively treating NO as a Σ state, which we denote as $|\chi\rangle$. The 5×5 interaction matrix in a molecular frame defined with the departing O atom on the positive z-axis and the NO molecule in the $x - z$ plane is given by [26,34]

$$V_{\mu\mu'}(R_c, \gamma) = \langle \chi\lambda\mu|\hat{V}|\chi\lambda\mu'\rangle = \sum_{l_A l_B m_A} (-1)^{l_A + \lambda - \mu} \times \frac{\langle\chi|\hat{Q}_{I_A,0}|\chi\rangle\langle\lambda||\hat{Q}^{l_B}||\lambda\rangle}{R^{l_A+l_B+1}} \left[\frac{(2l_A + 2l_B + 1)!}{(2l_A)!(2l_B)!}\right] \times \begin{pmatrix} l_A & l_B & l_A + l_B \\ m_A & -m_A & 0 \end{pmatrix} \begin{pmatrix} \lambda & l_B & \lambda \\ -\mu & -m_A & \mu' \end{pmatrix} c_{l_A m_A}(\gamma, 0). \quad (15)$$

The eigenvalues of this matrix yield the adiabatic long range potentials and the $|m|$-populations are obtained from the corresponding eigenvectors. In the Appendix, we show that for the $O(^1D_2)$ atom only the reduced quadrupole moment $\langle\lambda||\hat{Q}^{(l_B=2)}||\lambda\rangle$ is nonzero and that it is negative. The absolute value of $\langle\lambda||\hat{Q}^{l_B=2}||\lambda\rangle$ does not affect the corresponding eigenvectors.

For the diatom we include the dipole, quadrupole, octupole, and hexadecapole moments $\langle\chi|\hat{Q}_{l_A,0}|\chi\rangle$, $l_A = 1, 2, 3, 4$. The values were obtained from an ab initio calculation using the Gaussian 98 program package [35]. The NO molecule was placed along the z-axis, with the center of mass at the origin and the N atom on the positive z-axis and the NO distance equal to the experimental value of $r_0 = 2.18a_0$ [36]. The two components of the $X^2\Pi$ state were computed in a state averaged full valence complete active space self consistent field (CASSCF) calculation with an augmented correlation consistent polarized valence triple zeta (aug-cc-pVTZ) one electron basis [37]. The Gaussian package computes the Cartesian components of the multipole moments. The conversion to spherical components is straightforward as decribed, e.g., in Appendix E of reference [38].

The crucial assumption in the model is that upon excitation the system proceeds adiabatically on some potential surface until a critical atom-diatom separation R_c is reached, beyond which the interaction is too weak to affect the atomic polarization. This is, of course, a simplification because in reality there will be a transition region rather than a transition point between the short range adiabatic and long range diabatic regions.

Despite the numerous previous studies on the photodissociation of NO_2 above the second dissociation limit described in the Introduction, it is not certain which adiabatic potential leads to the $O(^1D_2)$ product. Therefore, we will present below the results for the full range of the angle γ for all five states included in the model.

5 Results from the semi-classical model

In the model described above there are three independent parameters for each channel: the anisotropy parameter β_v and the relative populations p_1/p_0 and p_2/p_0 . To find the best fit we varied β_v from –1 to 2 in steps of 0.01 and we also varied the populations in steps of 0.01 and for each case we computed the error as

$$\left(\frac{1}{4}\int_{-1}^{1}\sum_{J_f=1,3}|I_{ion}^{experiment}(J_f,J_i)-I_{ion}^{model}|^2 d\cos\theta\right)^{\frac{1}{2}}. \quad (16)$$

We include the factor of 1/4 because the range of integration is [–1,1] and two images contribute. The Legendre moments of the measured $O(^1D_2)$ ion images for $v = 1$, 2, 3, and 4 for both detection schemes are given in Table 3. The anisotropy parameters β_v and the fragment polarizations obtained from fitting these images with equation (11) are given in Table 4. In Figure 5 we compare the measured angular distributions with the fit. For $v = 2$, 3, 4 we obtain good fits with the errors as defined in equation (16) of about 0.025. As described above we determined the best fit by trying all possible values of β_v and populations $\tilde{p}_m$. With this procedure we can not only determine the value of β_v for which the total fit error is the smallest, but we also find the values of β_v for which either the error in the $^1P_1 \leftarrow {}^1D_2$ image or the error in the $^1F_3 \leftarrow {}^1D_2$ is smallest. For $v = 2$, 3, and 4 the values of β_v obtained in this way differ by less than 0.04. For $v = 1$, however, the error in the simultaneous fit is about 0.1 and the values of β_1 for which the individual images fit best differ by about 0.5. It seems that for this case at least one of the assumptions leading to equation (11) is not valid and we will not consider the $v = 1$ result further in developing the electrostatic model.

Table 3. The Legendre moments $\tilde{c}_l = c_l/c_0$ of the measured $O(^1D_2)$ ion images for both detection schemes.

	$^1P_2 \leftarrow {}^1D_2$			$^1F_3 \leftarrow {}^1D_2$		
v	$\tilde{c}_2$	$\tilde{c}_4$	$\tilde{c}_6$	$\tilde{c}_2$	$\tilde{c}_4$	$\tilde{c}_6$
1	2.108	0.922	0.320	0.565	0	0
2	1.038	−0.222	−0.174	0.632	−0.046	−0.013
3	1.013	−0.482	−0.152	0.389	−0.115	−0.001
4	0.406	−0.050	0.033	0.341	−0.066	0.050

Table 4. The anisotropy parameters β_v and the populations p_m obtained from fitting the measured $O(^1D_2)$ angular distributions with equation (11). The multipole moments of the density matrix $\rho_{0,RF}^{(k)}$ are related to the populations by equation (10). Note that $\rho_{0,RF}^{(0)} = 1/\sqrt{2J_i+1} = 1/\sqrt{5}$.

v	β_v	p_0	p_1	p_2	$\rho_0^{(2)}$	$\rho_0^{(4)}$
1	1.28	0.18	0.82	0	−0.32	−0.26
2	0.89	0.35	0.37	0.28	−0.14	0.11
3	0.79	0.46	0.32	0.22	−0.21	0.20
4	0.38	0.23	0.39	0.38	−0.02	0.02

l_A	$Q_{l_A,0}$
1	−0.0937
2	−0.8490
3	−0.9523
4	−0.6394

Table 5. Calculated multipole moments of $NO(^2\Pi)$ in atomic units.

The calculated multipole moments averaged over the two components of the NO $^2\Pi$ state that were used as input to the electrostatic model are given in Table 5. The experimental value for the dipole moment of the ground state is 0.0158 D ≈ 0.00622 a.u. and the $N^{\delta-}O^{\delta+}$ polarity is found in all high level ab initio calculations.

The potentials obtained by diagonalizing the interaction matrix (Eq. (15)) for $R_c = 5a_0$ are shown in Figure 6. Note that all the potentials shown would split into an A' and an A'' potential if the $^2\Pi$ character of NO would be taken into account. The choice of $R_c = 5a_0$ is rather arbitrary. We found, however, that qualitatively the shape

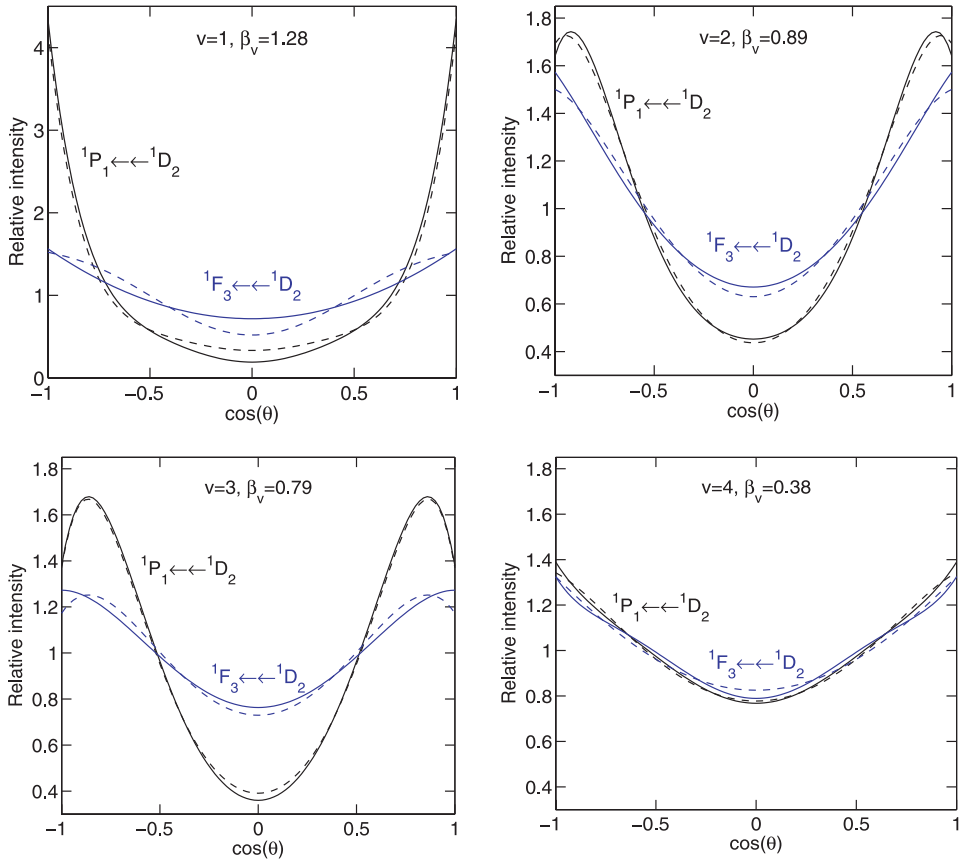

Fig. 5. The experimental $I_{ion}(\theta)$ (solid lines) for both detection schemes and the fit as described in Section 5 (dashed lines).

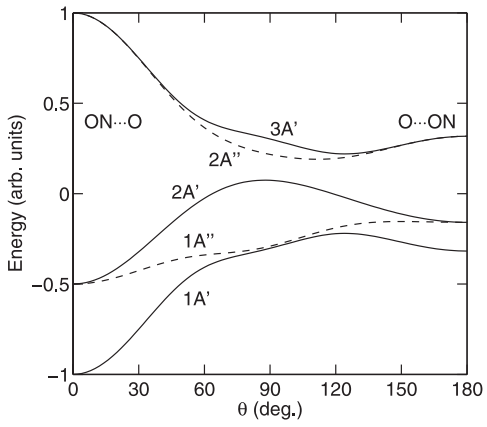

Fig. 6. The adiabatic potentials obtained as the eigenvalues of the interaction matrix [Eq. (15)] for $R_c = 5a_0$.

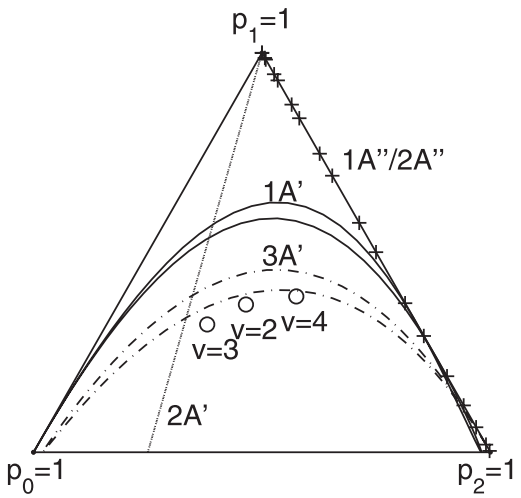

Fig. 7. The fragment polarizations for all five states corresponding to the potentials of Figure 6 for all values of the Jacobi angle γ. The three corners of the triangle correspond to fragments with pure $p_m = 1$ for $m = 0$, 1, and 2, and for an arbitrary point in the triangle the population p_m is proportional to the distance to the side opposite to the $p_m = 1$ corner. The A'' states have $p_0 = 0$ and are shown on the side marked with the + signs. The solid line corresponds to the $1A'$ state, the dotted line to the $2A'$ state and the dash-dot line to the $3A'$ state. The fragment polarizations derived from the fit to the experimental images for $v = 2$, 3, and 4 are indicated by circles.

of the potentials and the fragment polarizations derived from the model are quite insensitive to the choice of R_c.

For each of the five eigenvectors of the interaction matrix we obtain the relative populations p_1/p_0, and p_2/p_0 for each value of the Jacobi angle $\gamma = 0 \cdots 180°$. Since the sum of the populations is equal to 1 we can graphically represent the computed and measured fragment polarization as points in an equilateral triangle as shown in Figure 7. In Figure 8 we plot the computed $|m|$-populations as a function of the Jacobi angle γ.

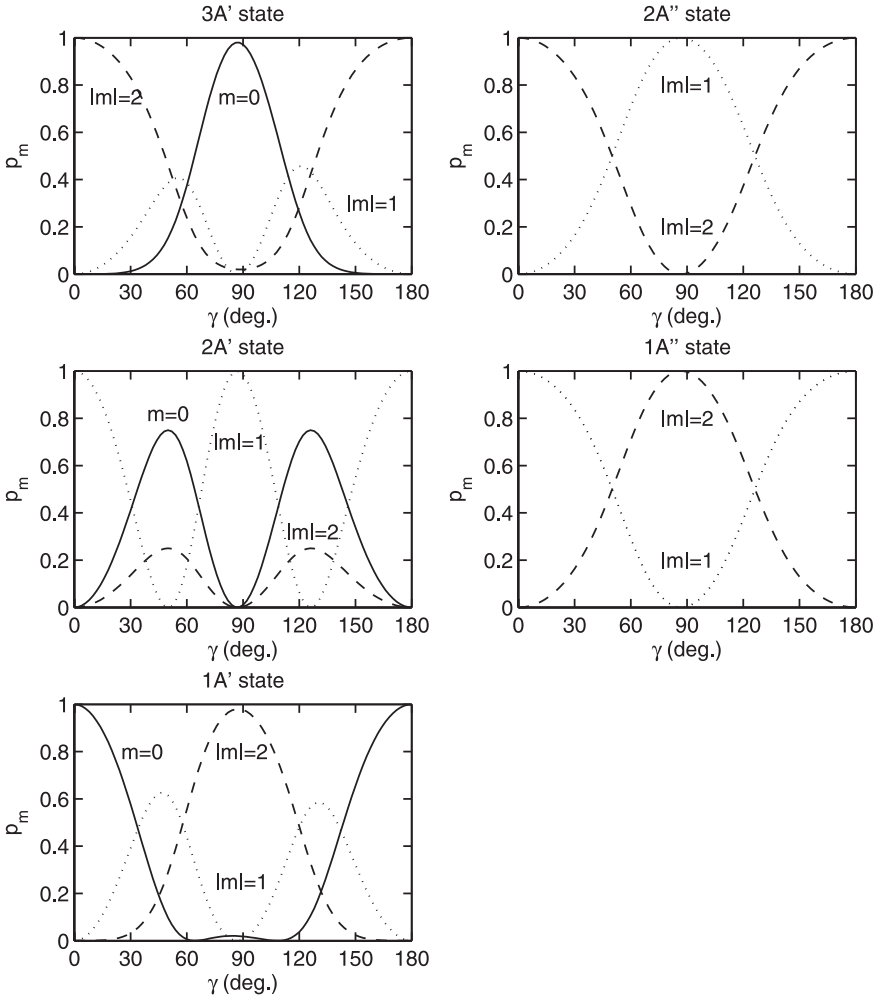

Fig. 8. The populations p_m for the A' and A'' states as a function of the Jacobi angle γ.

5.1 Discussion

If only the fragment polarization is considered, Figure 7 suggests that the observed polarizations could be accounted for by dissociation on the $3A'$ surface. However, this state in the model corresponds to the two most repulsive states correlating with the $NO(X^2\Pi)$ + $O(^1D_2)$ limit. From the limited amount of information in the literature on the states that correlate with $O(^1D_2)$ [39] it seems more likely that around 205 nm the $1A'$ model state is involved. In Tables 2 and 4 (experiment and fit) we see that the $v = 4$ channel has the lowest β parameter (0.38) and the lowest $m = 0$ population (0.23) [ignoring the $v = 1$ state because the fit was not good, presumably, as we have mentioned, due to the breakdown of one or more of the assumptions leading to equation (11)]. On kinematic grounds, a lower value of the anisotropy parameter most probably corresponds to a larger bending (and a larger angle γ). Examination of Figure 8 shows that only for the $1A'$ state is p_0 a decreasing function with respect to γ (for the range $0 < \gamma < 60°$, thereafter it shows a small secondary maximum at $\gamma = 90°$). Furthermore, from Figure 7 it is clear that if we take an average over a range of angles, the $1A'$ curve approaches the observations for $v = 2$, 3, and 4. Averaging has no effect for the $2A'$ and the A'' states. If more than one potential contributes to the $O(^1D_2)$ product these arguments are, of course, no longer valid.

6 Summary

In this paper we have presented the findings of a study concerned with the photodissociation dynamics of the NO_2 molecule in a one laser experiment for both reactions (1, 2). It was found from the present work that $O(^1D)$ product using photons resonant with the $3p'^1P_1$–$^1D_2$ or $3p'^1F_3$–$^1D_2$ transition is produced via $^2B_2/^2A_1$ parallel transition. For the transition $3p'^1P_1$–$^1D_2$, anisotropy parameter β was found to be 1.1 which is not in agreement with the experimental results presented by both Shafer et al. [17] and Demyanenko et al. [10]. The $3p'^1F_3$–$^1D_2$ transition product was studied for the first time and the anisotropy parameter was found to be very different than the $3p'^1P_1$–$^1D_2$ transition, due to the different polarization sensitivities at 200 nm.

Our experimental results for $O(^3P)$ channel are in good agreement with the experimental results by Ahmed et al. [19]. It was necessary to keep the gas pressure and the concentration of NO_2 very low in order to obtain a good image resolution.

DHP, GCG and MAC acknowledge support by the Dutch National Science Foundation CW-NWO. This work is partly supported by the European Community through the PICNIC network (Product Imaging and Correlation: Non-adiabatic Interactions in Chemistry) under contract number HPRN-CT-2002-00183.

Appendix: $O(^1D_2)$ quadrupole moment

In a one determinant approximation the $|\lambda\mu\rangle = |2,2\rangle$ state of $O(^1D_2)$ is given by $|1s\overline{1s}2s\overline{2s}2p_0\overline{2p_0}2p_1\overline{2p_1}|$. Since the s orbitals do not contribute to the quadrupole moment we find that

$$\langle|22|\hat{Q}_{2,0}|22\rangle = 2\langle 2p_0|\hat{Q}_{2,0}|2p_0\rangle + 2\langle 2p_1|\hat{Q}_{2,0}|2p_1\rangle.$$

The angular part of the atomic integrals can be evaluated analytically and the integrals can be expressed in terms of the expectation value $\langle r^2\rangle$: $\langle 2p_0|\hat{Q}_{2,0}|2p_0\rangle = (-2/5)\langle r^2\rangle$ and $\langle 2p_1|\hat{Q}_{2,0}|2p_1\rangle = (1/5)\langle r^2\rangle$, and we find $\langle 22|\hat{Q}_{2,0}|22\rangle = (-2/5)\langle r^2\rangle$. The reduced quadrupole moment is implicitly defined by the Wigner-Eckart theorem

$$\langle\lambda\mu|\hat{Q}_{l_B,m_B}|\lambda\mu'\rangle = (-1)^{\lambda-\mu}\begin{pmatrix}\lambda & l_B & \lambda\\ -\mu & m_B & \mu'\end{pmatrix}\langle\lambda||\hat{Q}^{(l_B)}||\lambda\rangle.$$

Evaluating the 3-j symbol gives $\langle\lambda||\hat{Q}^{l_B}||\lambda\rangle = -\sqrt{14/5}\langle r^2\rangle$, and so it must be negative.

References

1. R. Jost, J. Nygård, A. Pasinski, A. Delon, J. Chem. Phys. **105**, 1287 (1996); T.J. Butenhoff, E.A. Rohlfing, J. Chem. Phys. **98**, 5469 (1993)
2. G.E. Busch, K.R. Wilson, J. Chem. Phys. **56**, 3626 (1972)
3. G.E. Busch, K.R. Wilson, J. Chem. Phys. **56**, 3638 (1972)
4. H. Zacharias, M. Geilhaupt, K. Meier, K.H. Welge, J. Chem. Phys. **74**, 218 (1981)
5. T.G. Slanger, W.K. Bischel, M.J. Dyer, J. Chem. Phys. **79**, 2231 (1983)
6. J. Miyawaki, T. Tsuchizawa, K. Yamanouchi, S. Tsuchiya, Chem. Phys. Lett. **165**, 168 (1990); J. Miyawaki, K. Yamanouchi, S. Tsuchiya, Chem. Phys. Lett. **180**, 287 (1991)
7. A. Eppink, B.J. Whitaker, E. Gloaguen, B. Soep, A.M. Coroiu, D.H. Parker, J. Chem. Phys. **121**, 7776 (2004)
8. V.P. Hradil, T. Suzuki, S.A. Hewitt, P.L. Houston, B.J. Whitaker, J. Chem. Phys. **99**, 4455 (1993)
9. S.I. Ionov, G.A. Brucker, C. Jaques, Y. Chen, C. Wittig, J. Chem. Phys. **99**, 3420 (1993); D. Stolyarov, E. Polyakova, I. Bezel, C. Wittig, Chem. Phys. Lett. **358**, 71 (2002); I. Bezel, D. Stolyarov, C. Wittig, J. Phys. Chem. A **103**, 10268 (1999)
10. A.V. Demyanenko, V. Dribinski, H. Reisler, H. Meyer, C.X.W. Qian, J. Chem. Phys. **111**, 7383 (1999)
11. K.E.J. Hallin, A.J. Merer, Can. J. Phys. **54**, 1157 (1976)
12. K. Tsuji, M. Ikeda, J. Awamura, A. Kawai, K. Shibuya, Chem. Phys. Lett. **374**, 601 (2003)
13. R. Fan, L.D. Ziegler, J. Raman Spectrosc. **25**, 497 (1994)
14. M.R. Taherian, T.G. Slanger, J. Chem. Phys. **81**, 3796 (1984); M.R. Taherian, P.C. Cosby, T.G. Slanger, J. Phys. Chem. **91**, 2304 (1987)
15. W.M. Uselman, E.K.C. Lee, J. Chem. Phys. **65**, 1948 (1976)
16. R.C. Richter, V.I. Khamaganov, A.J. Hynes, Chem. Phys. Lett. **319**, 341 (2000)
17. N. Shafer, K. Tonokura, Y. Matsumi, S. Tasaki, M. Kawasaki, J. Chem. Phys. **95**, 6218 (1991)
18. M. Ahmed, D.S. Peterka, A.G. Suits, in *Atomic and Molecular Beams*, edited by R. Campargue (Springer-Verlag, Berlin, Germany, 2001), p. 343
19. M. Ahmed, D.S. Peterka, A.S. Bracker, O.S. Vasyutinskii, A.G. Suits, J. Chem. Phys. **110**, 4115 (1999)
20. W. Schneider, G.K. Moortgat, G.S. Tyndall, J.P. Burrows, J. Photochem. Photobiol. A-Chem. **40**, 195 (1987)
21. S.-M. Wu, A.M. Coroiu, I. Anton-Garcia, D.H. Parker, manuscript in preparation
22. Y.X. Mo, H. Katayanagi, M.C. Heaven, T. Suzuki, Phys. Rev. Lett. **77**, 830 (1996)
23. J.D. Geiser, S.M. Dylewski, J.A. Mueller, R.J. Wilson, R. Toumi, P.L. Houston, J. Chem. Phys. **112**, 1279 (2000)
24. D.W. Neyer, A.J.R. Heck, D.W. Chandler, J.M. Teule, M.H.M. Janssen, J. Phys. Chem. A **103**, 10388 (1999)
25. J.M. Teule, G.C. Groenenboom, D.W. Neyer, D.W. Chandler, M.H.M. Janssen, Chem. Phys. Lett. **320**, 177 (2000)
26. M. Brouard, R. Cireasa, A.P. Clark, T.J. Preston, C. Vallance, G.C. Groenenboom, O.S. Vasyutinskii, J. Phys. Chem. A **108**, 7965 (2004)
27. H. Katayanagi, T. Suzuki, Chem. Phys. Lett. **360**, 104 (2002)
28. R.F. Delmdahl, D.H. Parker, A. Eppink, J. Chem. Phys. **114**, 8339 (2001)
29. A.T.J.B. Eppink, D.H. Parker, Rev. Sci. Instrum. Sept. **68**, 3477 (1997)
30. V. Dribinski, A. Ossadtchi, V.A. Mandelshtam, H. Reisler, Rev. Sci. Instrum. **73**, 2634 (2002)
31. Y.X. Mo, T. Suzuki, J. Chem. Phys. **109**, 4691 (1998)
32. R.N. Zare, Mol. Photochem. **4**, 1 (1972)
33. K. Blum, *Density Matrix Theory and Applications* (Kluwer Academic, 1996)
34. A.J.H.M. Meijer, G.C. Groenenboom, A. van der Avoird, J. Chem. Phys. **101**, 7603 (1994)
35. M.J. Frisch, G.W. Trucks, H.B. Schlegel, G.E. Scuseria, M.A. Robb, J.R. Cheeseman, J. Montgomery, J.A.T. Vreven, K.N. Kudin, J.C. Burant, J.M. Millam, S.S. Iyengar, J. Tomasi, V. Barone, B. Mennucci, M. Cossi, G. Scalmani, N. Rega, G.A. Petersson, H. Nakatsuji, M. Hada, M. Ehara, K. Toyota, R. Fukuda, J. Hasegawa, M. Ishida, T. Nakajima, Y. Honda, O. Kitao, H. Nakai, M. Klene, X. Li, J.E. Knox, H.P. Hratchian, J.B. Cross,

V. Bakken, C. Adamo, J. Jaramillo, R. Gomperts, R.E. Stratmann, O. Yazyev, A.J. Austin, R. Cammi, C. Pomelli, J.W. Ochterski, P.Y. Ayala, K. Morokuma, G.A. Voth, P. Salvador, J.J. Dannenberg, V.G. Zakrzewski, S. Dapprich, A.D. Daniels, M.C. Strain, O. Farkas, D.K. Malick, A.D. Rabuck, K. Raghavachari, J.B. Foresman, J.V. Ortiz, Q. Cui, A.G. Baboul, S. Clifford, J. Cioslowski, B.B. Stefanov, G. Liu, A. Liashenko, P. Piskorz, I. Komaromi, R.L. Martin, D.J. Fox, T. Keith, M.A. Al-Laham, C.Y. Peng, A. Nanayakkara, M. Challacombe, P.M.W. Gill, B. Johnson, W. Chen, M.W. Wong, C. Gonzalez, J.A. Pople, Gaussian 98 (Gaussian Inc., 1998)

36. G. Hezberg, *Molecular Spectra and Molecular Structure: I. Spectra of Diatomic Molecules* (van Nostrand, New York, 1950)
37. T.H. Dunning, J. Chem. Phys. **90**, 1007 (1989); R.A. Kendall, T.H. Dunning, R.J. Harrison, J. Chem. Phys. **96**, 6796 (1992); D.E. Woon, T.H. Dunning, J. Chem. Phys. **100**, 2975 (1994)
38. A.J. Stone, *The Theory of Intermolecular Forces*. (Oxford University Press, Oxford, 1996)
39. M. Braunstein, J.W. Duff, J. Chem. Phys. **113**, 7406 (2000); V. Kurkal, P. Fleurat-Lessard, R. Schinke, J. Chem. Phys. **119**, 1489 (2003)